scientific reports

Check for updates

OPEN

Combination of THU/ALK-5i exhibits profound anti-MASH activity through suppression of lipogenesis and fibrogenesis

Kampeebhorn Boonloh[1], Eun Soo Lee[2], Su Ho Jo[4,5], Na Won Park[5], So Bin Lee[4,5] & Choon Hee Chung[3,4]✉

Metabolic dysfunction associated steatohepatitis (MASH), a progressive liver disease marked by steatosis, inflammation, and hepatocyte damage, is characterized by fibrosis, largely mediated by transforming growth factor-β (TGF-β). This study evaluated, as proof-of-concept, the therapeutic potential of tetrahydrocurcumin (THU), a curcumin derivative, in combination with EW-7197, an ALK-5 inhibitor, against MASH progression on in vitro and in vivo models. In vitro, TGF-β-treated hepatocytes (AML-12) and stellate cells (LX-2) were exposed to THU (1 μM), EW-7197 (0.5 μM), or their combination. EW-7197 mitigated TGF-β-induced hepatocyte morphological changes, while THU, alone or combined with EW-7197, reduced pathological lipid accumulation and counteracted EW-7197's adverse effects. In vivo, male C57BL/6J mice fed a methionine-choline deficient (MCD) diet for six weeks received oral EW-7197 (20 mg/kg) and THU (100 mg/kg). Co-administration effectively reduced liver fibrosis, improved MAFLD, and attenuated liver injury in MASH mice model. These findings suggest that the combination of THU and EW-7197 represents a promising therapeutic strategy for MAFLD/MASH by attenuating both liver fibrosis, and steatohepatitis more effectively than either monotherapy. While these findings highlight a synergistic anti-MASH effect of THU and EW-7197, the study is positioned as proof-of-concept. Further validation in metabolically relevant models (e.g., HFD/HFHC) and pharmacokinetic analyses are warranted before clinical translation can be considered.

Keywords Metabolic dysfunction associated steatohepatitis (MASH), ALK5 inhibitor, Tetrahydrocurcumin, TGF-β, Fibrosis

Metabolic dysfunction associated steatotic liver disease has become the leading cause of chronic liver disease, with a continuously rising global prevalence[1]. The disease spectrum encompasses a variety of states, including simple steatosis, steatohepatitis, liver fibrosis, and ultimately cirrhosis[2,3]. The initial metabolic disturbance triggers hepatic steatosis, while a subsequent pathogenic stimulus promotes oxidative stress, lipid peroxidation, inflammation, and ultimately liver injury and fibrosis[2,4]. It is well established that chronic low-grade inflammation and oxidative stress can trigger endoplasmic reticulum (ER) stress[5], further upregulating Srebp-1c, and contributing to hepatic lipid accumulation[6–8]. Thus, attenuating oxidative stress, reducing inflammatory responses, and inhibiting *de novo* lipogenesis represent promising therapeutic strategies for mitigating MAFLD progression.

Hepatic stellate cells (HSCs) are the primary source of collagen in the liver[9,10]. In MASH, these cells become activated and upregulate the expression of genes associated with hepatic fibrogenesis, such as α-smooth muscle actin (α-SMA) and collagen 1 A (Col1A)[10–12]. Growing evidence suggests the involvement of multiple signaling pathways in MASH pathogenesis, with the transforming growth factor-β (TGF-β) pathway playing a critical role[13]. TGF-β exerts diverse effects on cellular processes, including cell survival, proliferation, fibrosis, and

[1]Department of Pharmacology, Faculty of Medicine, Khon Kaen University, Khon Kaen 40002, Thailand. [2]Department of Otorhinolaryngology, Research Institute of Hearing Enhancement, Yonsei University Wonju College of Medicine, Wonju 26426, Republic of Korea. [3]Department of Internal Medicine and Global Medical Science, Yonsei University Wonju College of Medicine, Wonju 26426, Republic of Korea. [4]Research Institute of Metabolism and Inflammation, Yonsei University Wonju College of Medicine, Wonju 26426, Republic of Korea. [5]Department of Graduate Program for the Next Generation Global Leaders in Biomedical Science, Yonsei University Wonju College of Medicine, Wonju 26426, Republic of Korea. ✉email: cchung@yonsei.ac.kr

tumorigenesis[14]. Notably, TGF-β signaling contributes to the fibrogenic response during HSCs activation and is a key driver of MAFLD progression to MASH[12]. Upon ligand binding, the TGF-β receptor activates the Smad2/3-dependent pathway, which has been linked to extracellular matrix (ECM) protein production and fibrogenesis[12,15].

Targeting TGF-β signaling holds promise for the prevention and treatment of fibrotic diseases. Direct inhibition of the TGF-β type I receptor or activin-like kinase 5 (ALK-5), has emerged as a potential therapeutic strategy. Studies have shown that ALK-5 inhibitors can effectively block TGF-β-mediated pro-fibrotic effects[16]. These inhibitors competitively bind to the ATP-binding site of ALK-5, thereby inhibiting its catalytic activity[16,17]. EW-7197 (vactosertib) is a small-molecule ALK-5 inhibitor with demonstrated efficacy in improving various fibrotic conditions, including those affecting the kidney[18,19], lung[20], breast[20], and liver[21]. Mechanistically, EW-7197 regulates nuclear factor erythroid 2-related factor 2 (Nrf2), and heme oxygenase-1 (HO-1) levels and exerts its antifibrotic effects through TGF-β signaling inhibition[21,22].

Tetrahydrocurcumin (THU), is the primary metabolite of curcumin obtained from *Curcuma Longa*. THU possesses more favorable pharmacokinetic properties than curcumin, exhibiting greater plasma stability and enhanced bioavailability following oral administration[23,24]. These kinetic properties contribute to their potential applications in promoting longevity and combating various diseases, such as atherosclerosis[25], hypertension[19], nephrotoxicity[19,26], and metabolic disease[27,28]. Studies have demonstrated that THU has superior hypoglycemic activity compared to curcumin. In a rodent model of type 2 diabetes, THU effectively reduced plasma insulin levels, normalized blood glucose levels, and decreased hepatic gluconeogenic enzyme activity in diabetic mice[29]. Additionally, THU has demonstrated superior efficacy in downregulating cyclooxygenase-2 (COX-2) and nuclear factor-κB (NFkB)[30]. However, despite its promise in the treatment of metabolic disorders, such as diabetes and dyslipidemia, scientific evidence for the therapeutic efficacy of THU in obesity and hepatic steatosis is limited.

Intervention at the earliest stages of MAFLD is critical to disrupt the complex interplay and impede the progression to its more severe form, MASH. The development of effective MASH therapies remains challenging due to multifaceted pathophysiology. While lifestyle modifications are foundational, pharmacological interventions are frequently necessary. An ideal MASH therapy would possess multifactorial properties, including lipid-lowering, anti-inflammatory, and antifibrotic effects[31]. However, current pharmacological treatments often involve polypharmacy[32], leading to potential side effects and limited patient adherence. Consequently, herbal medicines, are emerging as promising complementary therapies. Such combination therapies may enhance treatment efficacy by reducing the dosage of standard medications, thereby mitigating the risk of drug-related adverse events. To this end, we aimed to investigate the potential of co-administering EW-7197 and THU to mitigate cellular and metabolic stress on the in vitro and in vivo MASH model. We hypothesized that this combination therapy would attenuate inflammation, reduce steatosis, and inhibit fibrogenesis, thereby preventing MASH progression.

Materials and methods

Chemical and reagents

The TGF-β receptor I inhibitor, EW-7197 (N-[4-([1,2,4]-triazolo[1,5-a] pyridine-6-yl)−5-(6-methylpyridin-2-yl)−1 H-imidazol-2-yl] methyl]−2-fluoro aniline), was synthesized at Uchem Inc. (Shanghai, China). The compound was dissolved in dimethyl sulfoxide (DMSO; Kanto Chemical Co., Tokyo, Japan). Tetrahydocurcumin (THU) was generously provided by the Government Pharmaceutical Organization (Bangkok, Thailand), and Dulbecco's modified Eagle's medium (DMEM), Dulbecco's modified Eagle's medium/Ham's Nutrient Mixture F-12 (DMEM/F-12; 1:1 ratio), and fetal bovine serum (FBS) were obtained from HyClone Laboratories Inc. (Logan, UT, USA). Penicillin/streptomycin (P/S) solution and palmitic acid (PA) were purchased from Sigma-Aldrich (St. Louis, MO, USA). BODIPY (4,4-Difluoro-1,3,5,7,8-Pentamethyl-4-Bora-3a,4a-Diaza-s-Indacene) was obtained from Thermo Fisher Scientific (Rockford, IL, USA). RIPA lysis buffer and a protease inhibitor cocktail were procured from Sigma-Aldrich (St. Louis, MO, USA).

Cell culture

Cell culture was conducted under a controlled environment of 37 °C with 5% CO_2 and saturated humidity in atmospheric air (95% air). The culture medium was replaced every alternate day. Alpha mouse liver 12 (AML-12) cells, representing normal mouse hepatocytes were obtained from American Type Culture Collection (ATCC). The cells were maintained in Dulbecco's Modified Eagle's Medium/Nutrient Mixture F-12 (DMEM/F-12; Corning Inc., Corning, NY, USA) supplemented with 10% fetal bovine serum (FBS; Gibco, NY, USA), 1% penicillin-streptomycin (Invitrogen, MA, USA), 1% insulin-transferrin-selenium (ITS) supplement (Gibco, NY, USA), and 40 ng/mL dexamethasone. Human hepatic stellate cells (LX-2) were purchased from MilliporeSigma™ and were cultured in DMEM supplemented with high glucose (4,500 mg/L d-glucose), l-glutamine (110 mg/L), sodium bicarbonate, sodium pyruvate, 10% FBS, and 1% penicillin-streptomycin.

Hepatocellular fibrosis was modeled by treating AML-12 or LX-2 cells with TGF-β at a concentration of 5 ng/mL for 24 h. The cells were then exposed to EW-7197 (0.5 μM), THU (1 μM), a combination of both, and no treatment (CON). Following treatment, whole-cell lysates were prepared for further analysis.

Immunofluorescence assay

AML-12 cells were treated as described previously; subsequently; the cells were fixed with BD Cytofix™ fixation buffer (BD Bioscience, NJ, USA) for 15 min at room temperature (24 ± 2 °C). Following fixation, cells were washed with phosphate-buffered saline (PBS) and permeabilized with 0.1% Triton X-100 (T8787, Sigma-Aldrich, MO, USA) for 20 min. To detect α-smooth muscle actin (α-SMA), cells were incubated overnight at 4 °C with anti-α-SMA primary antibody (Santa Cruz, CA, USA) diluted 1:200 in 3% bovine serum albumin

(BSA). After washing, the cells were incubated with Alexa Fluor 488-conjugated mouse anti-IgG secondary antibody (Cell Signaling Technology, Danvers, MA, USA) diluted 1:500 in 3% BSA for 2 h at room temperature. The cells were then washed twice with PBS and stained with 10 ng/mL 4′,6-diamidino-2-phenylindole (DAPI) solution (Abcam, CB, UK) for 15 min at room temperature for nuclear staining. Finally, cells were washed twice with PBS and mounted using Immu-Mount™ mounting medium (Thermo Fisher Scientific, MA, USA). Fluorescence images were captured using a laser scanning confocal microscope (Carl Zeiss Microscopy GmbH, Oberkochen, Germany).

BODIPY staining

Following treatment, the cells were fixed with 4% formaldehyde for 30 min at room temperature and washed with PBS. Subsequently, the cells were incubated with 1 μM BODIPY 493/503 staining solution (Thermo Fisher Scientific, MA, USA) for 30 min at 37 °C in a dark room. After two washes with PBS, the cells were mounted on slides using Immu-Mount™ mounting medium (FS9990402, Fisher Scientific, MA, USA). Stained cells were visualized under an LSM 800 confocal fluorescence microscope (Carl Zeiss Microscopy GmbH, Oberkochen, Germany). Lipid droplet count, and droplet intensity per cell were evaluated and quantified using ImageJ (Fiji) software, version 1.53c (National Institutes of Health, Bethesda, MD, USA).

Animal model of MASH

All animal procedures were approved by the Institutional Animal Care and Use Committee of Yonsei University Wonju College of Medicine (Approval Number: YWC-221020-1). All experimental operations were conducted in accordance with the relevant regulations and the ARRIVE guidelines (https://arriveguidelines.org). Briefly, eight -week-old male C57BL/6J mice (20–25 g body weight) were obtained from Daehan BioLink Co., Ltd. (Eumseong, Korea). After a one-week acclimatization period under standard laboratory conditions with unrestricted access to food and water *(ad libitum)*, the mice were randomly assigned to five experimental groups (n = 10/group): normal control (CON), MCD control, MCD-THU (100 mg/kg), MCD-EW-7197 (20 mg/kg), and MCD-THU + EW-7197. All groups, except the normal control group, were fed an MCD diet. In the MCD-THU group, THU was directly incorporated into the MCD diet. In the EW-7197 group, the compound was dissolved in a solution mimicking artificial concentrated gastric juice according to our previous study[19] (prepared with 900 mL of dd H_2O, 2.0 g of NaCl, 3.2 g of pepsin, and 7 mL of concentrated HCl) that was diluted 1:10 with phosphate-buffered saline. This diluted solution was administered by oral gavage to the normal control and MCD control groups as a vehicle, while the MCD-EW-7197 group received a dose of 20 mg/kg EW-7197 via the same route throughout the experiment.

At the end of the experiment, mice were anesthetized with 250 mg/kg 2,2,2-tribromoethanol (Avertin, T48402; Sigma-Aldrich, St. Louis, MO, USA) by intraperitoneal injection. Following anesthesia and confirmation of absent deep reflexes, a thoracotomy will be performed to collect blood via cardiac puncture, after which the animal will be euthanized. The serum, and liver tissues were collected and stored at −80 °C or fixed in a fixation buffer for subsequent pathological and biochemical analyses. The downstream analyses were designed to assess the efficacy of THU and EW-7197 in alleviating MAFLD progression.

Metabolic parameters and biochemical analysis

During the terminal phase of the experiment, serum total cholesterol (TC), aspartate aminotransferase (AST), and alanine aminotransferase (ALT) levels were quantified using commercially available reagent kits (Asan Pharm, Hwaseong, Korea), following the manufacturer's instructions. The process involves both enzymatic and colorimetric methods. Hepatic triglyceride (TG) content was determined by liver homogenate analysis. Briefly, 200 mg of minced liver tissue was homogenized and extracted in 1 mL of NP-40 lysis buffer. The homogenates were then centrifuged at 10,000 rpm for 10 min at 4 °C. Following centrifugation, the collected supernatants were used to measure TG concentration using enzymatic and colorimetric methods from a commercially available triglyceride assay kit (Cayman Chemical, MI, USA), according to the manufacturer's protocol. Hepatic TG levels were expressed as milligrams per deciliter per gram of liver tissue (mg/dL/g).

Histological assessment and scoring

The isolated mouse livers were excised and fixed overnight at room temperature in 10% formaldehyde. Subsequently, the tissues were embedded in paraffin blocks and sectioned to a thickness of 8 μm using a rotary microtome. Hematoxylin and eosin (H&E) staining was used to assess steatosis and lobular inflammation, while Masson's Trichrome staining was performed to evaluate fibrosis. Histological scoring was conducted in a blinded manner according to the NAFLD activity score system (NAS), which integrates the following components: steatosis (0–3), lobular inflammation (0–3), and hepatocellular ballooning (0–2). Quantitative analysis of steatotic area and fibrotic area were visualized using a charge-coupled device (CCD) equipped with an optical microscope (Pulnix; Orleans Drive, Sunnyvale, CA, USA) to reduce observer bias, in line with ARRIVE guidelines.

Western blot analysis

Whole-cell lysates were prepared from cultured cells or frozen liver tissues using RIPA buffer (Elpis Biotech, Korea) supplemented with a phosphatase and protease inhibitor cocktail (Pierce, IL, USA). Lysates were centrifuged at 12,000 rpm for 30 min at 4 °C. The supernatants were collected and stored at −80 °C for further analysis. The protein concentration was determined using a bicinchoninic acid (BCA) protein assay kit (Pierce, IL, USA). Equal amounts of protein (20 μg) were separated by sodium dodecyl sulfate-polyacrylamide gel electrophoresis (SDS-PAGE) on 8–12% gels and transferred onto polyvinylidene difluoride (PVDF) membranes (Millipore, MA, USA). The membranes were blocked with 5% skim milk in Tris-buffered saline containing 0.1% Tween-20 (TBST) to minimize non-specific binding. Primary antibodies were diluted 1:1000 in 5% BSA and

incubated with the membranes overnight at 4 °C. The following antibodies were used: α-smooth muscle actin (α-SMA; SC-32251), collagen type I (Col1A; SC-293182), connective tissue growth factor (CTGF; SC-101586), sterol regulatory element-binding protein-1c (Srebp-1c; #SC-13551), fatty acid synthase (Fasn; SC-55580), monocyte chemoattractant protein-1 (MCP-1; SC-28879), interleukin-1β (IL-1β; SC-12742), and β-actin (SC-47778), which purchased from Santa Cruz Biotechnology (CA, USA). Additionally, antibodies for Smad2/3 (#3102), AMPK (#2532), and NFκB (#4764) and their phosphorylated counterparts (p-Smad3; #9520, p-AMPK; #2531, p-NFκB; #3033) were obtained from Cell Signaling Technologies (Danvers, MA, USA).

Following primary antibody incubation, the membranes were washed with TBST and incubated with horseradish peroxidase (HRP)-conjugated secondary antibodies (dilution 1:1,000 in 5% BSA). Protein bands were visualized using an enhanced chemiluminescence (ECL) solution (Elpis-Biotech, Daejeon, Korea), according to the manufacturer's instructions. The band intensity was quantified using ImageJ software version 1.50i (National Institutes of Health, Bethesda, MD, USA). Protein expression levels were normalized by considering β-actin (a housekeeping gene) expression levels.

Statistical analysis

Data are presented as mean ± standard error of the mean (SEM) throughout this study. Statistical analyses were performed using the Prism software (version 8.0; GraphPad Software Inc., San Diego, CA, USA). One-way analysis of variance (ANOVA) followed by Tukey's multiple comparison test was used to assess the differences among multiple groups. Statistical significance was set at $P < 0.05$.

Results

EW-7197 relieves hepatocellular fibrosis

To assess the antifibrotic actions of the compounds, experiments were conducted in human hepatic stellate LX-2 cells. Stimulation with TGF-β (5 ng/mL) induced marked upregulation of extracellular matrix (ECM) proteins, including α-SMA, Col1A, and CTGF, through activation of the canonical TGF-β/Smad2/3 pathway (Fig. 1A–E). THU monotherapy did not produce statistically significant suppression of ECM protein expression in TGF-β-stimulated LX-2 cells, although a downward trend was observed, particularly the protein expression of α-SMA (Fig. 1D-E). In contrast, treatment with EW-7197, either alone or in combination with THU, markedly

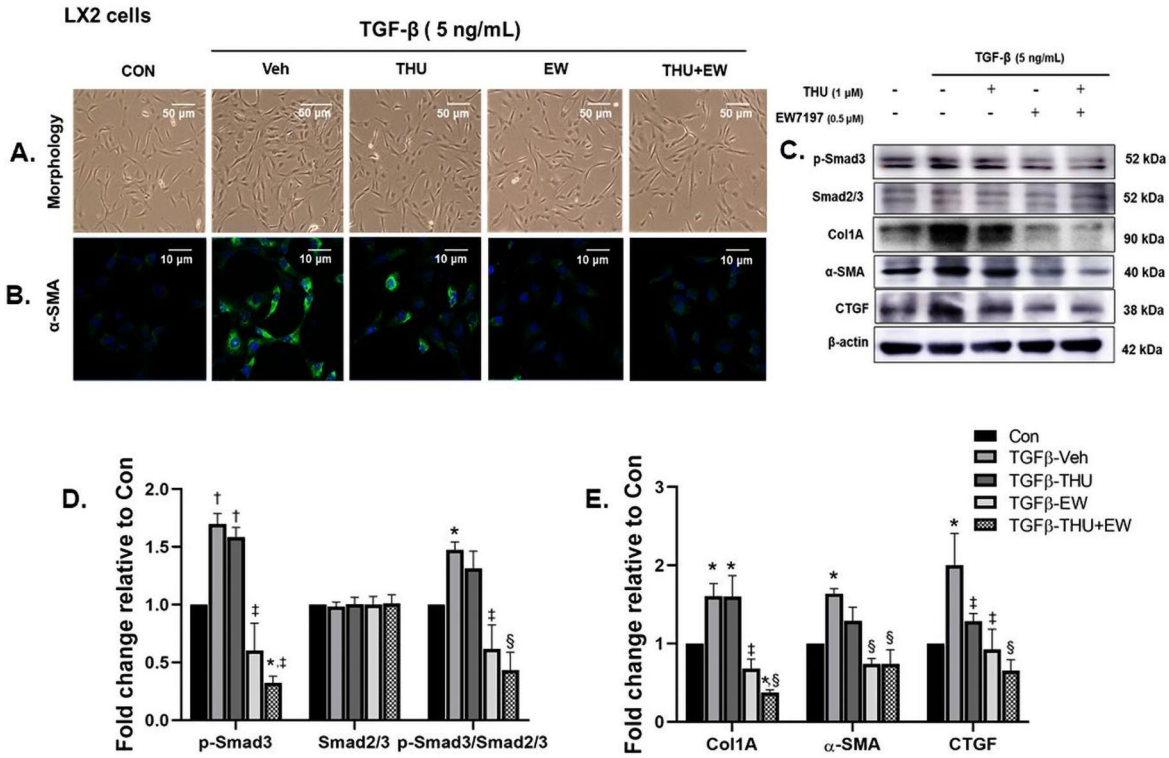

Fig. 1. EW-7197 suppresses hepatic fibrosis in LX-2 cells. Cellular morphology after treatment (**A**). α-SMA staining (**B**). Expression of p-Smad3 and the downstream proteins (Col1A, α-SMA, and CTGF) in the canonical pathway (**C**). Representative bar graphs of p-Smad3 and its downstream profibrotic proteins (**D**, **E**). $^{*}p < 0.05$, $^{\dagger}p < 0.01$ vs. CON group, $^{\ddagger}p < 0.05$, $^{\S}p < 0.01$ vs. TGF-β control group. Values are presented as the means ± SEM.

reduced ECM protein expression, most notably α-SMA and Col1A ($p < 0.01$). Among the treatment groups, the THU + EW-7197 combination achieved the most pronounced antifibrotic effect (Fig. 1B–E).

The combination treatment of THU and EW-7197 potentiates antifibrotic effects on MCD-induced MASH mice

In line with the in vitro model, the MCD-fed mice model of MASH (Fig. 2A) mirrored these findings. EW-7197 and combination therapy of THU and EW-7197 demonstrated potent antifibrotic effects in MASH mice. These treatments suppressed ECM protein levels via the canonical p-Smad2/3 pathway (Fig. 2B, C, D). While THU also exhibited a trend towards decreased ECM protein levels, these reductions were not statistically significant for some of the proteins investigated (CTGF, $p = 0.067$).

Our recent finding furnishes additional evidence supporting the augmentation of antifibrotic effects through combination therapy. Notably, this approach resulted in a significant reduction of α-SMA expression ($p < 0.01$), particularly evident in the context of various extracellular matrix proteins (Fig. 2B, D).

THU improves hepatic injury in the MASH model

MCD feeding induced a clear MASH phenotype, characterized by extensive hepatic lipid droplet accumulation (Fig. 3A), increased hepatic TG content (Fig. 3C), enhanced ECM deposition (Fig. 3B), and elevated serum AST and ALT levels (Fig. 3D, E). Treatment with THU markedly attenuated hepatic steatosis, as evidenced by a reduction in lipid droplet area, decreased hepatic TG, and lower steatosis scores (Fig. 3A, C, F, I). However, its antifibrotic effect was modest and did not reach statistical significance. In contrast, EW-7197 treatment markedly attenuated ECM deposition and reduced fibrotic area (Fig. 3B, G) while exerting only minor effects on steatosis (Fig. 3F, I). Notably, combination therapy with THU and EW-7197 produced the most pronounced histological improvements, with concurrent reductions in steatosis, lobular inflammation, and fibrosis (Table 1). These effects were reflected in significantly lower NAS scores compared with either monotherapy (Fig. 3H).

EW-7197 relieves in vitro hepatocellular damages with a mild derangement in lipid metabolism

Aligned with the experiments conducted in hepatic stellate cells, we found that EW-7197 effectively inhibits the expression of profibrotic markers in hepatocytes; p-Smad3, Col1A, α-SMA, and CTGF, and is more effective

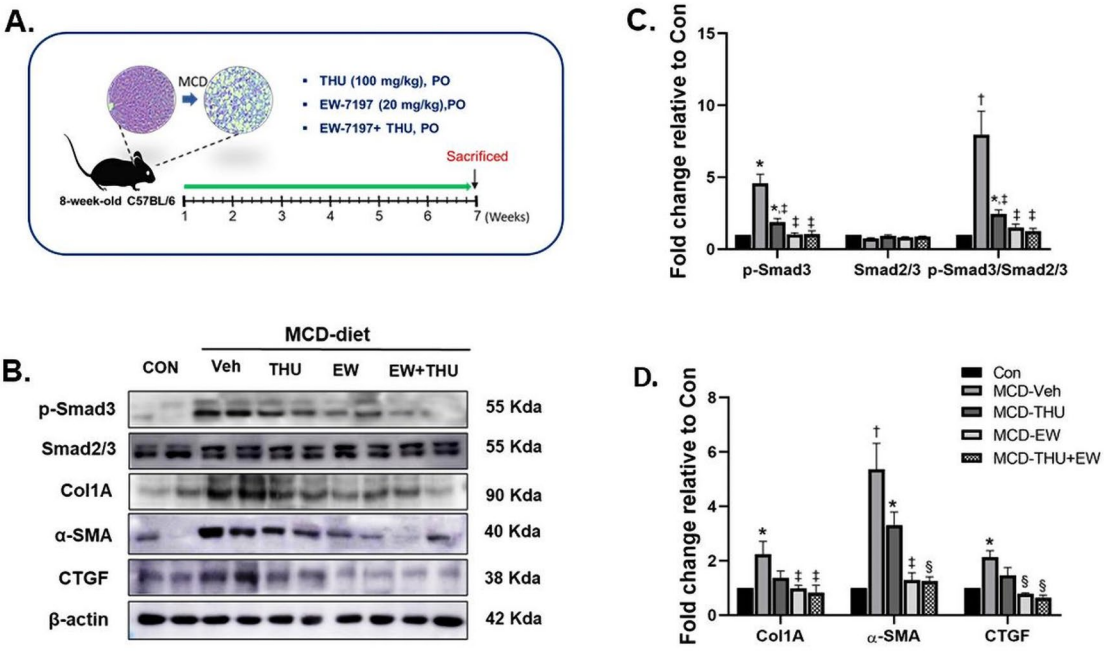

Fig. 2. The combination treatment of THU and EW-7197 potentiates antifibrotic effects on MCD-fed mice. Experimental design of animal model (**A**). Expression of p-Smad3 and the downstream proteins (Col1A, α-SMA) in the canonical pathway (**B**). Representative bar graphs of p-Smad2/3 and downstream profibrotic proteins (**C**, **D**). $^{*}p < 0.05$, $^{\dagger}p < 0.01$ vs. CON group, $^{\ddagger}p < 0.05$, $^{\S}p < 0.01$ vs. MCD-control group. Values are presented as the means ± SEM.

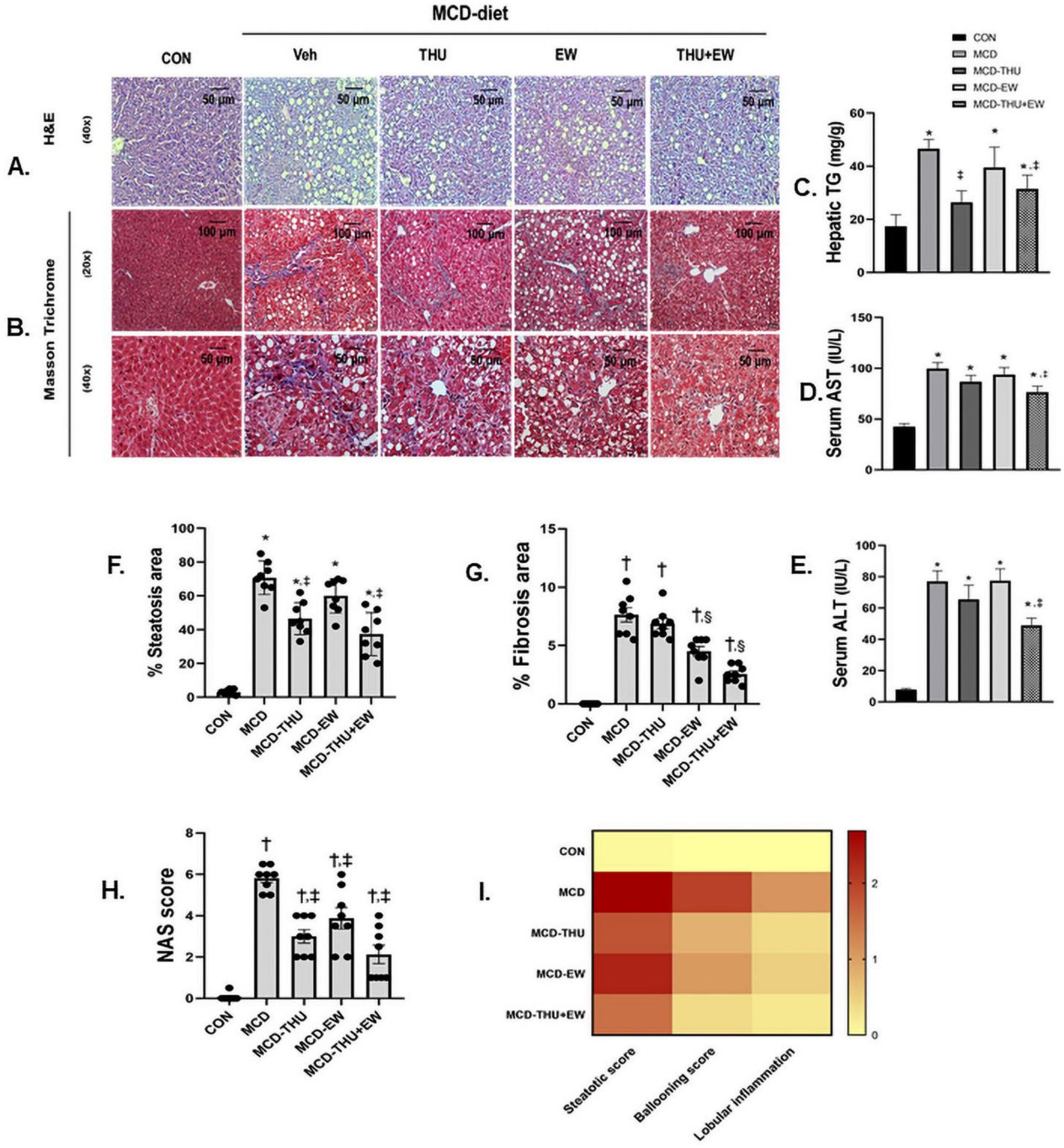

Fig. 3. THU improves hepatic injury in the MASH model. Hepatic H&E staining (**A**). Hepatic Masson's Trichrome staining (**B**). Hepatic TG level (**C**). Serum AST levels (**D**). Serum ALT levels (**E**). Steatosis area (**F**). Fibrosis area (**G**). NAS score (**H**). Heatmap analysis of NAS features (**I**). $^{*}p < 0.05$, $^{\dagger}p < 0.01$ vs. CON group, $^{\ddagger}p < 0.05$, $^{\S}p < 0.01$ vs. PA-, or MCD-control group, ($n = 8$/group). Values are presented as the means ± SEM.

than THU. Furthermore, the combination therapy group exhibited the most prominent antifibrotic effects (Fig. 4C-F).

Interestingly, in the TGF-β-challenged AML-12 model, TGF-β induced morphological change, transforming the shape of this hepatocyte into fibroblast-like morphology (Fig. 4A). However, the EW-7197 treatment reversed these morphological alterations. Quantitative assessment of lipid droplet number per cell and BODIPY staining intensity revealed a marked increase in TGF-β–challenged AML-12 cells upon EW-7197 treatment, indicating an unfavorable effect on lipid accumulation (Fig. 4A-B and G–I; Supplementary Table 3 S). This was further corroborated by increased expression of the lipogenic genes Srebp-1c and Fasn (Fig. 4J, K). THU mitigated the undesirable effects of EW-7197 in hepatocytes. The co-treatment of THU and EW-7197 resulted in a decrease in

Group	Steatosis score	Lobular inflammation score	Ballooning score	%Steatosis area	% Fibrosis area	NAS score
CON	0.06 ± 0.06	0.00 ± 0.00	0.00 ± 0.00	2.25 ± 0.45	0.00 ± 0.00	0.06 ± 0.06
MCD-Vehicle	2.69 ± 0.16†	1.13 ± 0.13†	2.00 ± 0.00†	69.31 ± 3.29*	7.63 ± 0.61†	5.81 ± 0.21†
MCD-THU	1.81 ± 0.13†,§	0.38 ± 0.18*,‡	0.81 ± 0.13*,‡	46.25 ± 3.70*,‡	6.88 ± 0.44†	3.00 ± 0.33†,‡
MCD-EW	2.31 ± 0.13†	0.50 ± 0.16*,‡	1.06 ± 0.27†,‡	59.06 ± 3.16*	4.50 ± 0.42†,§	3.88 ± 0.52†,‡
MCD-THU + EW	1.50 ± 0.19*,‡	0.25 ± 0.16*,§	0.38 ± 0.16§	38.06 ± 4.67*,‡	2.56 ± 0.26†,§	2.13 ± 0.45†,‡

Table 1. Histological scoring and quantitative analysis of steatosis, inflammation, ballooning, fibrosis, and NAS in MCD–fed mice model. Histological scores (steatosis, lobular inflammation, and ballooning) were determined according to the NAS system, while percentage of steatosis and fibrosis area were quantified by morphometric analysis. $^{*}p < 0.05$, $^{\dagger}p < 0.01$ vs. CON group, $^{\ddagger}p < 0.05$, $^{\S}p < 0.01$ vs. MCD-control group. Values are presented as the means ± SEM.

both lipid droplets and lipogenic gene expression compared to that observed in EW-7197 monotherapy (Fig. 4B, I, J).

THU prevents the downregulation of p-AMPK and reduces lipid accumulation

To investigate the potential of THU in improving lipid metabolism, AML-12 cells were challenged with palmitic acid (PA). PA is a well-established lipotoxicity inducer in various cell types. Consistent with the findings of other research groups, PA induced cellular stress and enhanced lipid accumulation in AML-12 cells, as confirmed by microscopy and BODIPY staining (Fig. 5A, B). A significant increase in lipid droplets per cell, droplet area per cell, and BODIPY staining intensity per cell were observed in PA-treated groups. These signals were attenuated following treatment, most notably with THU, and were most markedly reduced under the combined treatment (Fig. 5A-E; Supplementary Table 4 S). While AMPK phosphorylation was reduced, Srebp-1c and Fasn were upregulated (Fig. 5F, G). THU treatment prevented the downregulation of p-AMPK, thereby suppressing the overexpression of Srebp-1c and Fasn, which are key players in lipogenesis.

THU displays anti-inflammatory effects

PA reportedly prompts an inflammatory response by augmenting the phosphorylation of NFκB. In line with this knowledge, our experiment showcased an elevation in p-NFκB levels, alongside its downstream targets IL-1β and MCP-1, in PA-exposed AML-12 cells (Fig. 6A, B). THU treatment suppressed p-NFκB and its downstream genes, which mitigate PA-induced cellular inflammation. These findings suggest that THU exerts anti-inflammatory effects. Although EW-7197 tended to shield cells against PA-induced inflammation, the reductions were not uniform across all downstream targets (Fig. 6A, B). The in vivo results obtained from MCD-fed mice model mirrored the in vitro observations. EW-7197 treatment alone displayed a trend towards anti-inflammatory effects by reducing p-NFκB levels. However, some of its downstream targets failed to reach statistically significant differences compared with the disease control group, particularly MCP-1(Fig. 6C, D). THU demonstrated a more potent anti-inflammatory effect than EW-7197. Taken together, the combination therapy exhibited superior anti-inflammatory activity compared to the monotherapy.

THU improves redox status and displays anti-apoptotic effects

Our findings revealed increased expression of NADPH oxidase 4 (NOX4), the enzyme responsible for the generation of reactive oxygen species (ROS), in AML-12 cells challenged with PA. Remarkably, treatment with THU, alone or in combination, effectively reversed these effects (Fig. 7A, B). Additionally, PA exposure increased the expression of Caspase-3, a crucial executor of apoptosis, and the pro-apoptotic Bax/Bcl-2 ratio (Fig. 7A, C). Intriguingly, both THU and combination therapy significantly decreased the expression of Caspase-3 and the Bax/Bcl-2 ratio, indicating reduced apoptosis. Although EW-7197 alone tended to reduce apoptosis, its effects were not statistically significant (Fig. 7C).

In the MCD-mice model of MASH, NOX4 expression is upregulated, whereas superoxide dismutase 2 (SOD2), an enzyme that counteracts ROS, is downregulated. These phenotypes induced by the MCD diet could be corrected by the administration of THU or a combination of THU and EW-7197 (Fig. 7D, E). Furthermore, Caspase-3 and the Bax/Bcl2 ratio, which were elevated in MCD-fed mice, were reduced in the groups treated with THU and combination therapy (Fig. 7D, F). Collectively, these results imply that THU improves the cellular redox state, thereby reducing cellular stress and apoptosis.

Discussion

Excessive hepatic lipid accumulation and a well-defined cascade involving oxidative stress, inflammation, and liver injury have been reported to pave the way for the development of MAFLD and MASH[4,33].

Liver fibrosis is a consequence of wound healing and prevents tissue breakdown during inflammation, apoptosis, and necrosis[10,34]. Early detection and intervention are crucial because of the silent progression and delayed onset of symptoms associated with liver fibrosis. Hepatic stellate cells (HSCs) reside in the space of Disse between hepatocytes and sinusoidal endothelial cells and exist in a quiescent state (qHSCs) under normal physiological conditions[9,11]. However, upon chronic liver injury, such as that induced by persistent inflammation and hepatocyte death, HSCs are activated (aHSCs)[12]. aHSCs majorly contribute to liver fibrosis by secreting ECM proteins, leading to the hallmark features of fibrosis[12,35]. This extensive ECM deposition

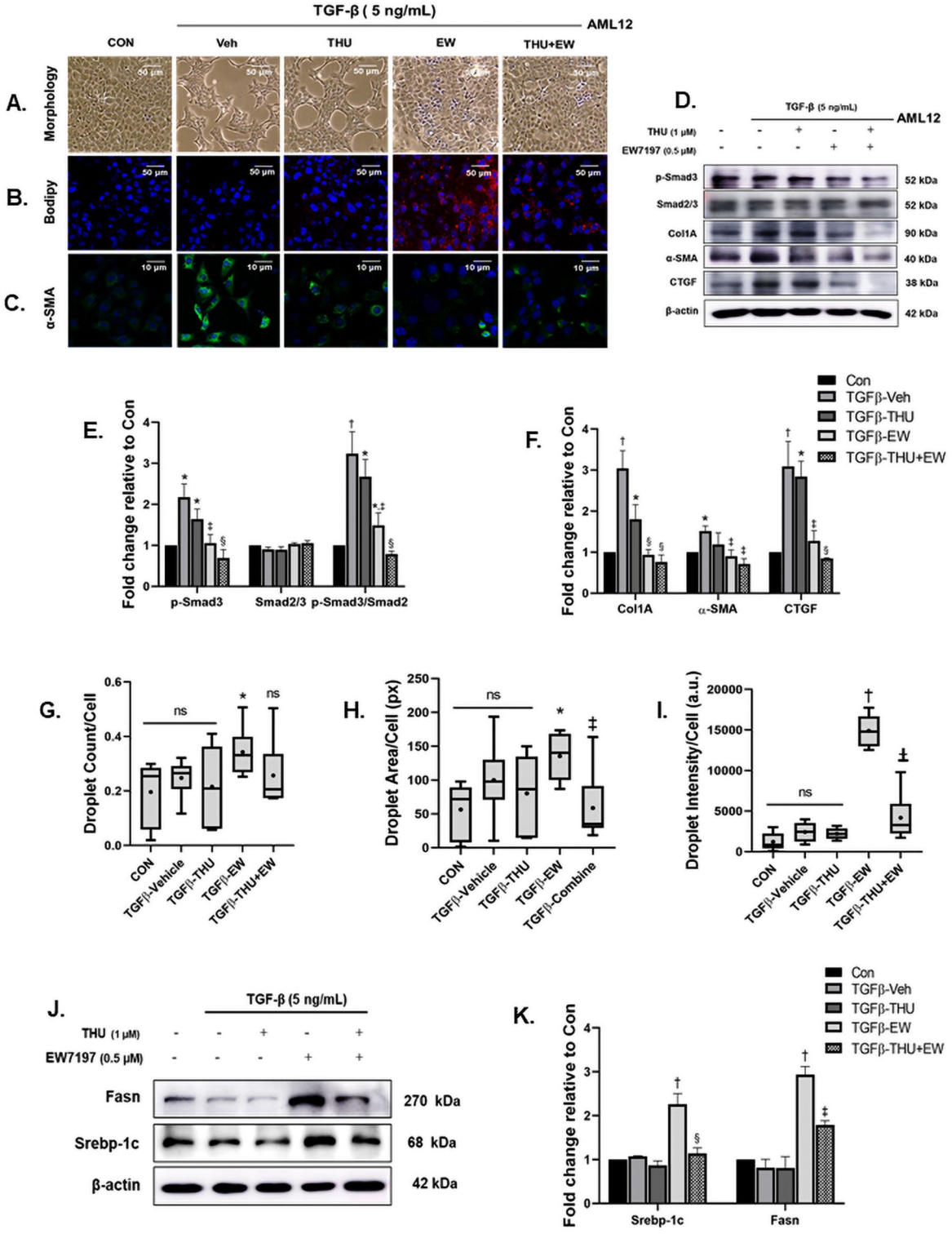

Fig. 4. EW-7197 attenuates hepatocellular fibrosis with lipid metabolism derangement in hepatocytes. Cellular morphology after treatment (**A**). BODIPY staining (**B**). α-SMA staining (**C**). Expression of p-Smad3 and the downstream proteins (Col1A, α-SMA, and CTGF) in the canonical pathway (**D**). Representative bar graphs of p-Smad3 and its downstream profibrotic proteins (**E**, **F**). Lipid droplet count/cell (**G**). Lipid droplet area/cell (**H**). Lipid droplet intensity/cell (**I**). Protein levels of lipogenic genes; Srebp-1c and Fasn (**J**). Representative bar graphs of the lipogenic genes (**K**). $^{*}p < 0.05$, $^{\dagger}p < 0.01$ vs. CON group, $^{\ddagger}p < 0.05$, $^{\S}p < 0.01$ vs. TGF-β control group, $^{t}p < 0.05$ vs. TGF-β plus EW group. px; pixels, a.u.; arbitrary units. Values are presented as the means ± SEM.

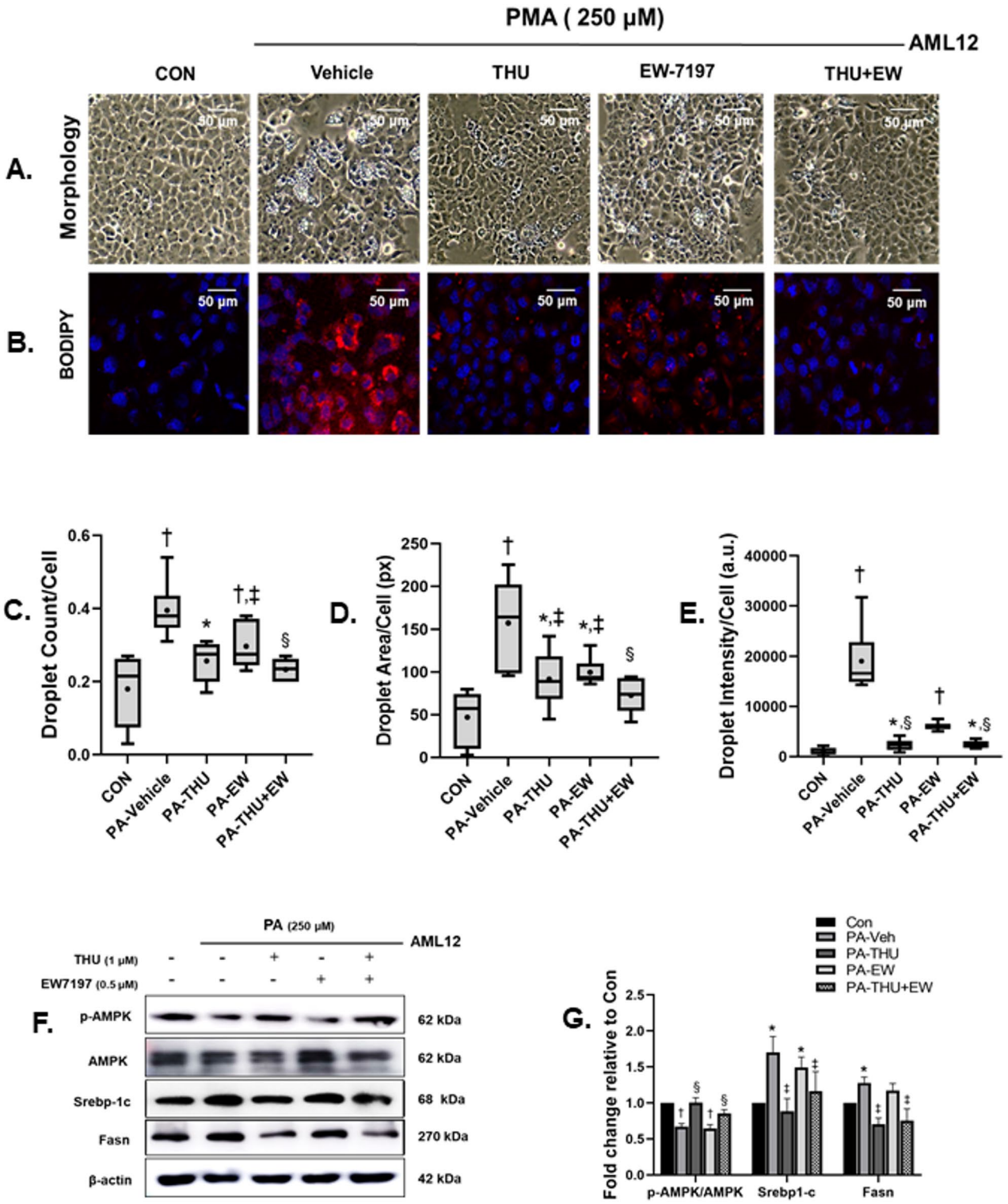

Fig. 5. THU diminishes hepatic lipid accumulation and prevents the downregulation of p-AMPK. Cellular morphology after treatment (**A**). BODIPY staining (**B**). Lipid droplet count/cell (**C**). Lipid droplet area/cell (**D**). Lipid droplet intensity/cell (**E**). Protein levels of p-AMPK, AMPK, and the lipogenic proteins; Srebp-1c and Fasn (**F**). Representative bar graphs of the lipogenic proteins (**G**). $^{*}p < 0.05$, $^{\dagger}p < 0.01$ vs. CON group, $^{\ddagger}p < 0.05$, $^{\S}p < 0.01$ vs. PA-control group. px; pixels, a.u.; arbitrary units. Values are presented as the means ± SEM.

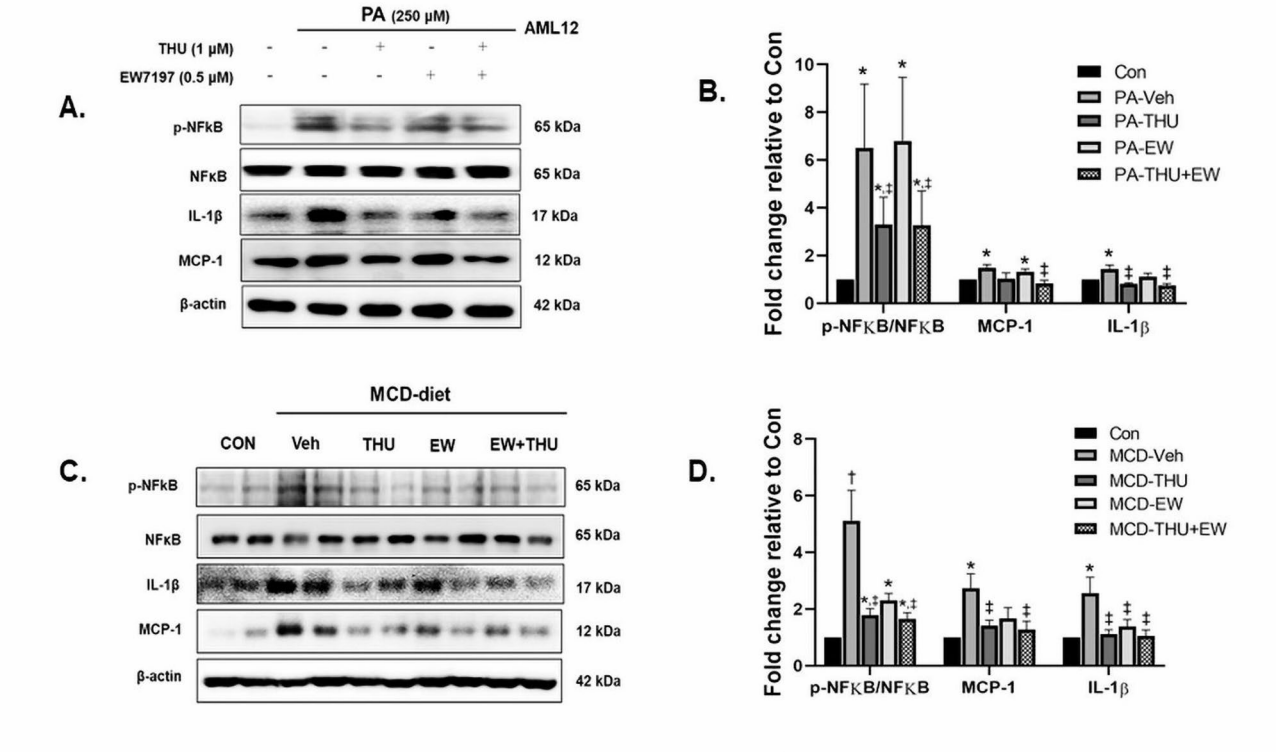

Fig. 6. THU displays anti-inflammatory effects. Protein levels of inflammatory markers in PA-induced AML-12 cells (**A**), from the liver tissue of MCD-fed mice (**C**), and representative bar graphs in both models (**B**, **D**). $^{*}p < 0.05$, $^{\dagger}p < 0.01$ vs. CON group, $^{\ddagger}p < 0.05$, $^{\S}p < 0.01$ vs. PA-, or MCD-control group. Values are presented as the means ± SEM.

disrupts the normal liver architecture and impairs its function[12,14,34]. TGF-β induces fibrosis in various organs by stimulating the production of collagen-rich ECM, a sign of progressive tissue fibrosis[13,14,18]. Our in vitro findings demonstrated that EW-7197 potently inhibits ECM protein upregulation (α-SMA, Col1A, CTGF) via the p-Smad2/3 canonical pathway, reversing TGF-β-induced morphological changes in hepatocytes. However, paradoxically, in TGFβ-challenged AML-12 cells, EW-7197 prevented TGFβ-induced morphological changes but simultaneously promoted intracellular lipid accumulation in hepatocytes. This effect was accompanied by upregulation of Srebp-1c and Fasn expression, representing an adverse response confined specifically to the in vitro hepatocyte model. Importantly, we did not detect overt toxicity or hepatocellular lipid accumulation in vivo attributable solely to EW-7197 monotherapy. These findings suggest that while EW-7197 possesses anti-fibrotic properties, it may unfavorably alter hepatocellular lipid metabolism under in vitro conditions. Notably, THU demonstrated lipid-lowering properties and mitigated these in vitro adverse effects when co-administered[36].

Our in vitro models do not capture the complex paracrine and juxtacrine interactions between hepatocytes and stellate cells, which are critical in MASH fibrogenesis[37]. While monocultures allowed us to isolate cell-type–specific responses and avoid species mismatch, we note that future work using co-culture or organoid systems will be necessary to validate these findings in a more physiologically relevant context. We acknowledge that α-SMA is not a canonical marker of hepatocyte activation; its induction under prolonged TGF-β exposure likely reflects cellular stress or dedifferentiation rather than hepatocyte-driven fibrogenesis[13]. In this study, α-SMA in AML-12 cells was used to indicate TGF-β–induced morphological changes, which were clearly observed (Fig. 4A). To ensure pharmacological consistency, we evaluated these changes alongside profibrotic gene modulation (α-SMA, Col1A, CTGF) in hepatic stellate cells, the primary readout for antifibrotic efficacy of THU and EW7197. Future work will include additional epithelial and mesenchymal markers (e.g., vimentin) to better characterize TGF-β–induced stress responses in hepatocytes.

To clarify the mechanistic role of THU in lipid metabolism, we employed a palmitic acid (PA)-induced lipotoxicity model in AML-12 hepatocytes. PA exposure increases lipid accumulation[27,28], triggers inflammatory responses[38,39], and induces ER stress[39]. THU treatment prevented PA-induced downregulation of p-AMPK and reduced SREBP-1c/Fasn expression. These findings are consistent with prior reports by Chen et al[27,40]., which demonstrated that THU activates AMPK, suppresses lipogenesis, and promotes fatty acid oxidation. In MCD-fed mice, THU similarly reduced hepatic lipid accumulation, likely through preservation of p-AMPK and suppression of lipogenic proteins. These findings support a role for THU in AMPK-mediated lipid lowering and ER stress protection, although definitive causality will require dose–response and mechanistic blockade studies.

Excessive ROS generation contributes to hepatic steatosis and mitochondrial dysfunction, creating a vicious cycle of oxidative stress. PA exacerbates this by disrupting lipid metabolism and activating the PKC/NOX4 pathway, while MCD-fed mice also exhibit NOX4-driven ROS production due to ER stress from nutrient

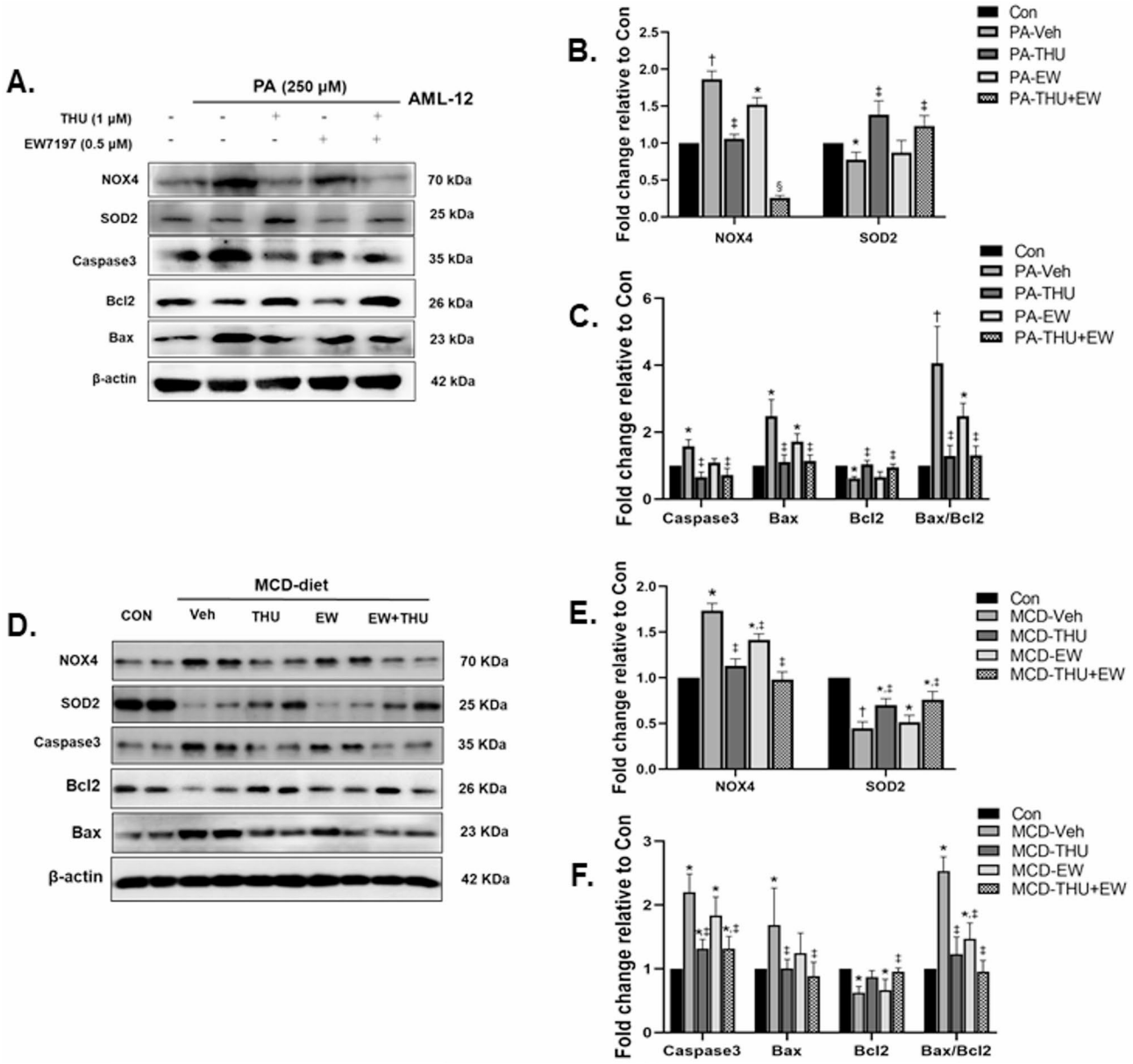

Fig. 7. THU refines redox status and exhibits antiapoptotic effects in vitro and in vivo models. Expression levels of oxidant-related and apoptotic genes in PA-induced AML-12 cells (**A**) in the liver tissue of MCD-fed mice (**D**). Representative bars in AML-12 cells (**B**, **C**) and MCD-fed mice (**E**, **F**) respectively. $^{*}p < 0.05$, $^{\dagger}p < 0.01$ vs. CON group, $^{\ddagger}p < 0.05$, $^{\S}p < 0.01$ vs. PA-, or MCD-control group. Values are presented as the means ± SEM.

deficiency. Our studies show that THU suppresses NOX4 expression and enhances SOD2, thereby restoring redox balance. EW-7197 showed only a modest effect, but the combination therapy yielded the strongest inhibition. Lipotoxicity in hepatocytes induces oxidative stress, mitochondrial dysfunction, c-JNK activation, and proinflammatory cytokine release, which activate TLR4 and perpetuate inflammation. Kupffer cell activation further amplifies this cascade via MCP-1 and IL-1β. In line with this, PA stimulation upregulated p-NFκB and downstream cytokines in vitro, while MCD feeding triggered oxidative stress and inflammation in vivo. THU significantly suppressed p-NFκB and proinflammatory gene expression, both alone and in combination with EW-7197, with the combination producing the most potent anti-inflammatory effect. Although our study focused on hepatocyte and stellate cell responses, immune cell–mediated inflammation is a key driver of MASH progression. Given that THU suppressed PA-induced NFκB activation in hepatocytes, it is plausible that THU may also modulate NFκB-dependent signaling in hepatic immune cells. Future work using Kupffer cells or hepatocyte–immune co-culture systems will be necessary to clarify this potential immunomodulatory effect.

Caspase-3, traditionally recognized as a pivotal executor of apoptosis, exacerbates liver injury, and disrupts tissue integrity, thereby contributing to the development of MASH[41]. Recent investigations have suggested that caspase-3 plays an intricate role in fibrogenesis[42]. Caspase-3 activation in endothelial cells can induce the release

of CTGF, which serves as a potent profibrotic factor, enhancing myofibroblast differentiation and ECM synthesis, thus fostering fibrosis[42]. Consistent results were obtained from our results in the PA-induced hepatocytes and MCD-fed mice model. THU demonstrated superior anti-apoptotic properties compared to EW-7197 alone, as evidenced by the reduction in caspase-3 expression and the Bax/Bcl2 ratio. Notably, the combination treatment group exhibited the most potent anti-apoptotic effects, as shown in Fig. 7.

Our present analysis primarily establishes apoptosis as the dominant mode of cell death, supported by caspase-3 activation and Bax/Bcl-2 modulation. This finding raises important hypotheses that merit further investigation. We recognize that targeted validation—such as GPX4 and ACSL4 expression, lipid ROS measurement, and ferrostatin-1 rescue for ferroptosis[43] or assessment of NLRP3 inflammasome activation, gasdermin D cleavage, and IL-1β secretion for pyroptosis[44]—would provide stronger mechanistic insights. We therefore highlight these assays as important future directions to complement our current apoptosis-focused findings.

The MCD diet is a well-established model of MAFLD/MASH, as it disrupts hepatic lipid metabolism by depleting methionine and choline, thereby impairing lipid export and leading to intracellular lipid accumulation[45]—hallmarks of hepatic steatosis[46,47]. Consistent with prior reports, our findings confirmed that the MCD diet effectively induces steatosis, as evidenced by elevated hepatic triglyceride content and characteristic histological features on H&E staining. We also acknowledge the limitations of the MCD-fed mice model. Notably, it does not recapitulate obesity or insulin resistance and alters hepatic CYP expression, including downregulation of CYP1A and CYP3A isoforms[48]. These aspects are particularly relevant in the context of THU, which has been reported to modulate CYP activity[49], raising the possibility of pharmacokinetic interactions with EW-7197. Therefore, the pharmacokinetic profiling will be included in future work to guide translational dosing. Our in vivo study, THU was administered at 100 mg/kg[26,27], and EW-7197 at 20 mg/kg[50], doses previously used in metabolic disease models that demonstrated bioactivity without overt toxicity. Although circulating THU levels were not quantified—limiting precise interpretation of systemic exposure and interaction potential—the selected dose falls within a therapeutic range that has been shown to exert beneficial effects, including improvements in glycemic control[29], lipid metabolism[27,28], and inflammation[26]. These factors may have influenced treatment outcomes and should be taken into account when considering translational relevance[36].

In the MASH mice model, MCD feeding significantly reduced food intake, body weight, and liver weight, while trend to increase the liver-to-body weight ratio. Treatment with THU, EW-7197, or their combination (THU + EW-7197) did not fully restore body weight or food intake, but partially improved liver-to-body weight ratios. Notably, the combination group showed a slight normalization trend compared with MCD alone (Supplementary data Table 1S, Fig. 5S). Histological evaluation showed reductions in steatosis area and NAS scores following treatment, with the THU + EW7197 combination producing the most pronounced improvements across steatosis, inflammation, and fibrosis. In contrast, changes in serum ALT and AST were modest (Supplementary data Table 2 S), likely reflecting the short feeding duration and the limited sensitivity of these biochemical markers to injury type. These results emphasize that while serum enzymes provide partial insights, quantitative histological endpoints remain critical for accurately assessing therapeutic efficacy in MASH. Although the MCD model does not reproduce obesity or insulin resistance, its capacity to induce severe steatosis, progressive fibrosis, hepatocellular injury, and marked elevations in hepatic triglyceride content makes it a valuable platform for mechanistic and therapeutic studies. Our findings provide proof of concept that interventions combining anti-steatotic and anti-fibrotic actions can yield meaningful disease improvement, supporting further translational exploration.

The present study demonstrates that combination therapy with THU and EW-7197 provides complementary benefits in both in vitro and in vivo the MCD-induced MASH model. Propose mechanisms are illustrated in Fig. 8. THU primarily attenuated steatosis and lipid accumulation, whereas EW-7197 targeted fibrogenic pathways by reducing ECM deposition. The combined regimen synergistically reduced steatosis, inflammation, and fibrosis, resulting in the most pronounced decrease in NAS scores. These findings underscore the value of multipronged therapeutic strategies in MASH, where targeting both lipid metabolism and fibrogenesis may achieve superior outcomes compared with single-pathway interventions.

Conclusion

In summary, our findings provide proof-of-concept evidence that the combination of THU and EW-7197 can concurrently target steatosis, inflammation, and fibrosis in MASH. THU primarily ameliorated lipid accumulation and inflammatory stress, while EW-7197 suppressed fibrogenic pathways, with the combination producing the most pronounced histological improvement in the MCD-fed mice model. However, validation in metabolically relevant models, pharmacokinetic profiling, and comparison with clinical benchmarks will be essential to substantiate translational potential.

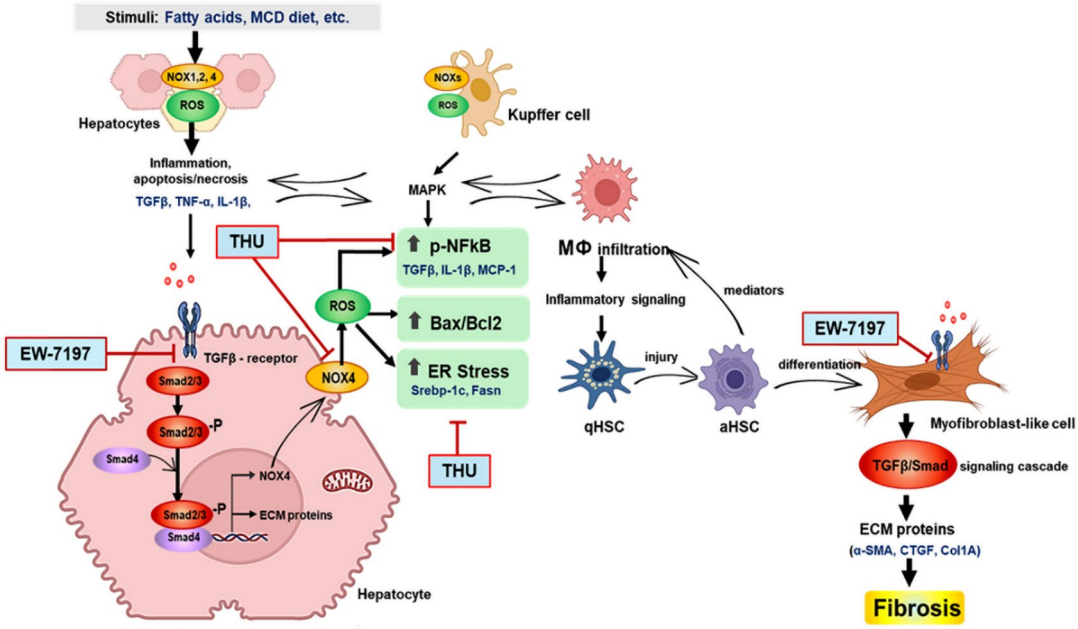

Fig. 8. Propose mechanisms of ALK5i/THU combination therapy in MASH model.

Data availability

The authors confirm that the data supporting the findings of this study are available within the article.The raw datasets generated and analyzed during this study have been deposited in a public repository and are accessible at: https://doi.org/10.6084/m9.figshare.30172507.

Received: 20 May 2025; Accepted: 8 October 2025
Published online: 14 November 2025

References

1. Labenz, C., Kostev, K., Alqahtani, S. A., Galle, P. R. & Schattenberg, J. M. Impact of non-alcoholic fatty liver disease on metabolic comorbidities in type 2 diabetes mellitus. *Exp. Clin. Endocrinol. Diabetes.* **130**, 172–177. https://doi.org/10.1055/a-1378-4679 (2022).
2. Pouwels, S. et al. Non-alcoholic fatty liver disease (NAFLD): a review of pathophysiology, clinical management and effects of weight loss. *BMC Endocr. Disord.* **22**, 63. https://doi.org/10.1186/s12902-022-00980-1 (2022).
3. Traussnigg, S. et al. Challenges and management of liver cirrhosis: practical issues in the therapy of patients with cirrhosis due to NAFLD and NASH. *Dig. Dis.* **33**, 598–607. https://doi.org/10.1159/000375353 (2015).
4. Tanase, D. et al. (ed, M.) The intricate relationship between type 2 diabetes mellitus (T2DM), insulin resistance (IR), and nonalcoholic fatty liver disease (NAFLD). *J. Diabetes Res.* **2020** 3920196 https://doi.org/10.1155/2020/3920196 (2020).
5. Hasnain, S. Z., Lourie, R., Das, I., Chen, A. C. & McGuckin, M. A. The interplay between Endoplasmic reticulum stress and inflammation. *Immunol. Cell. Biol.* **90**, 260–270. https://doi.org/10.1038/icb.2011.112 (2012).
6. Kim, J. Y. et al. ER stress drives lipogenesis and steatohepatitis via caspase-2 activation of S1P. *Cell* 175, 133–145 e115, (2018). https://doi.org/10.1016/j.cell.2018.08.020
7. Ye, J. et al. ER stress induces cleavage of membrane-bound ATF6 by the same proteases that process SREBPs. *Mol. Cell.* **6**, 1355–1364. https://doi.org/10.1016/s1097-2765(00)00133-7 (2000).
8. Xiao, T. et al. Mitochondrial stress protein HSP60 regulates ER stress-induced hepatic lipogenesis. *J. Mol. Endocrinol.* **64**, 67–75. https://doi.org/10.1530/JME-19-0207 (2020).
9. Zhang, M. et al. Hepatic stellate cell senescence in liver fibrosis: Characteristics, mechanisms and perspectives. *Mech. Ageing Dev.* **199**, 111572. https://doi.org/10.1016/j.mad.2021.111572 (2021).
10. Kisseleva, T. & Brenner, D. Molecular and cellular mechanisms of liver fibrosis and its regression. *Nat. Rev. Gastroenterol. Hepatol.* **18**, 151–166. https://doi.org/10.1038/s41575-020-00372-7 (2021).
11. Higashi, T., Friedman, S. L. & Hoshida, Y. Hepatic stellate cells as key target in liver fibrosis. *Adv. Drug Deliv Rev.* **121**, 27–42. https://doi.org/10.1016/j.addr.2017.05.007 (2017).
12. Kumar, S., Duan, Q., Wu, R., Harris, E. N. & Su, Q. Pathophysiological communication between hepatocytes and non-parenchymal cells in liver injury from NAFLD to liver fibrosis. *Adv. Drug Deliv Rev.* **176**, 113869. https://doi.org/10.1016/j.addr.2021.113869 (2021).
13. Dewidar, B., Meyer, C., Dooley, S. & Meindl-Beinker, A. N. TGF-beta in hepatic stellate cell activation and liver fibrogenesis-updated 2019. *Cells* **8** https://doi.org/10.3390/cells8111419 (2019).
14. Morikawa, M., Derynck, R. & Miyazono, K. TGF-beta and the TGF-beta family: context-dependent roles in cell and tissue physiology. *Cold Spring Harb Perspect. Biol.* **8** https://doi.org/10.1101/cshperspect.a021873 (2016).
15. Hu, H. H. et al. New insights into TGF-beta/Smad signaling in tissue fibrosis. *Chem. Biol. Interact.* **292**, 76–83. https://doi.org/10.1016/j.cbi.2018.07.008 (2018).
16. Ling, L. E. & Lee, W. C. Tgf-beta type I receptor (Alk5) kinase inhibitors in oncology. *Curr. Pharm. Biotechnol.* **12**, 2190–2202. https://doi.org/10.2174/138920111798808257 (2011).
17. Lin, A., Cai, Z., Hu, G. & Li, Q. Identification of ALK5 inhibitor via structure-based virtual screening and ADMET prediction. *J. Recept Signal. Transduct. Res.* **35**, 559–564. https://doi.org/10.3109/10799893.2015.1024852 (2015).

18. Moon, J. A., Kim, H. T., Cho, I. S., Sheen, Y. Y. & Kim, D. K. IN-1130, a novel transforming growth factor-beta type I receptor kinase (ALK5) inhibitor, suppresses renal fibrosis in obstructive nephropathy. *Kidney Int.* **70**, 1234–1243. https://doi.org/10.1038/sj.ki.5001775 (2006).
19. Joshi, P. et al. Role of Curcumin in ameliorating hypertension and associated conditions: a mechanistic insight. *Mol. Cell. Biochem.* **477**, 2359–2385. https://doi.org/10.1007/s11010-022-04447-8 (2022).
20. Park, C. Y. et al. EW-7195, a novel inhibitor of ALK5 kinase inhibits EMT and breast cancer metastasis to lung. *Eur. J. Cancer.* **47**, 2642–2653. https://doi.org/10.1016/j.ejca.2011.07.007 (2011).
21. Park, S. A. et al. EW-7197 inhibits hepatic, renal, and pulmonary fibrosis by blocking TGF-beta/Smad and ROS signaling. *Cell. Mol. Life Sci.* **72**, 2023–2039. https://doi.org/10.1007/s00018-014-1798-6 (2015).
22. Park, J., Choi, J., Cho, I. & Sheen, Y. Y. Radiotherapy-induced oxidative stress and fibrosis in breast cancer are suppressed by vactosertib, a novel, orally bioavailable TGF-beta/ALK5 inhibitor. *Sci. Rep.* **12**, 16104. https://doi.org/10.1038/s41598-022-20050-9 (2022).
23. Pan, M. H., Huang, T. M. & Lin, J. K. Biotransformation of Curcumin through reduction and glucuronidation in mice. *Drug Metab. Dispos.* **27**, 486–494 (1999).
24. Okada, K. et al. Curcumin and especially Tetrahydrocurcumin ameliorate oxidative stress-induced renal injury in mice. *J. Nutr.* **131**, 2090–2095. https://doi.org/10.1093/jn/131.8.2090 (2001).
25. Zhang, L. et al. Tetrahydrocurcumin-related vascular protection: an overview of the findings from animal disease models. *Molecules* **27** https://doi.org/10.3390/molecules27165100 (2022).
26. Sangartit, W. et al. Tetrahydrocurcumin ameliorates kidney injury and high systolic blood pressure in high-fat diet-induced type 2 diabetic mice. *Endocrinol. Metab. (Seoul).* **36**, 810–822. https://doi.org/10.3803/EnM.2021.988 (2021).
27. Pan, M. H. et al. Attenuation by Tetrahydrocurcumin of adiposity and hepatic steatosis in mice with high-fat-diet-induced obesity. *J. Agric. Food Chem.* **66**, 12685–12695. https://doi.org/10.1021/acs.jafc.8b04624 (2018).
28. Pari, L. & Murugan, P. Antihyperlipidemic effect of Curcumin and Tetrahydrocurcumin in experimental type 2 diabetic rats. *Ren. Fail.* **29**, 881–889. https://doi.org/10.1080/08860220701540326 (2007).
29. Pari, L. & Murugan, P. Effect of Tetrahydrocurcumin on blood glucose, plasma insulin and hepatic key enzymes in streptozotocin induced diabetic rats. *J. Basic. Clin. Physiol. Pharmacol.* **16**, 257–274. https://doi.org/10.1515/jbcpp.2005.16.4.257 (2005).
30. Zhang, Z. B. et al. Curcumin's metabolites, Tetrahydrocurcumin and octahydrocurcumin, possess superior anti-inflammatory effects in vivo through suppression of TAK1-NF-kappaB pathway. *Front. Pharmacol.* **9**, 1181. https://doi.org/10.3389/fphar.2018.01181 (2018).
31. Ratziu, V., Goodman, Z. & Sanyal, A. Current efforts and trends in the treatment of NASH. *J. Hepatol.* **62**, 65–75. https://doi.org/10.1016/j.jhep.2015.02.041 (2015).
32. Oseini, A. M. & Sanyal, A. J. Therapies in non-alcoholic steatohepatitis (NASH). *Liver Int.* **37** (Suppl 1), 97–103. https://doi.org/10.1111/liv.13302 (2017).
33. Farrell, G. C., Haczeyni, F. & Chitturi, S. Pathogenesis of NASH: how metabolic complications of overnutrition favour lipotoxicity and pro-inflammatory fatty liver disease. *Adv. Exp. Med. Biol.* **1061**, 19–44. https://doi.org/10.1007/978-981-10-8684-7_3 (2018).
34. Caligiuri, A., Gentilini, A., Pastore, M., Gitto, S. & Marra, F. Cellular and molecular mechanisms underlying liver fibrosis regression. *Cells* **10** https://doi.org/10.3390/cells10102759 (2021).
35. Hammerich, L. & Tacke, F. Hepatic inflammatory responses in liver fibrosis. *Nat. Rev. Gastroenterol. Hepatol.* **20**, 633–646. https://doi.org/10.1038/s41575-023-00807-x (2023).
36. Anwar, C., Chu, Y. C., Tsai, M. L., Ho, C. T. & Lai, C. S. Tetrahydrocurcumin alleviates di-(2-ethylhexyl) phthalate-induced adipose tissue dysfunction and testicular toxicity in adult mice: possible involvement of adiponectin-adipoR signaling in the testis. *Food Funct.* **16**, 583–600. https://doi.org/10.1039/d4fo04271a (2025).
37. Godoy, P. et al. Recent advances in 2D and 3D in vitro systems using primary hepatocytes, alternative hepatocyte sources and non-parenchymal liver cells and their use in investigating mechanisms of hepatotoxicity, cell signaling and ADME. *Arch. Toxicol.* **87**, 1315–1530. https://doi.org/10.1007/s00204-013-1078-5 (2013).
38. Ricchi, M. et al. Differential effect of oleic and palmitic acid on lipid accumulation and apoptosis in cultured hepatocytes. *J. Gastroenterol. Hepatol.* **24**, 830–840. https://doi.org/10.1111/j.1440-1746.2008.05733.x (2009).
39. Teixeira, F. S. et al. Differential lipid accumulation on HepG2 cells triggered by palmitic and Linoleic fatty acids exposure. *Molecules* **28** https://doi.org/10.3390/molecules28052367 (2023).
40. Chen, J. W. et al. Tetrahydrocurcumin ameliorates free fatty acid-induced hepatic steatosis and improves insulin resistance in HepG2 cells. *J. Food Drug Anal.* **26**, 1075–1085. https://doi.org/10.1016/j.jfda.2018.01.005 (2018).
41. Thapaliya, S. et al. Caspase 3 inactivation protects against hepatic cell death and ameliorates fibrogenesis in a diet-induced NASH model. *Dig. Dis. Sci.* **59**, 1197–1206. https://doi.org/10.1007/s10620-014-3167-6 (2014).
42. Laplante, P. et al. Caspase-3-mediated secretion of connective tissue growth factor by apoptotic endothelial cells promotes fibrosis. *Cell. Death Differ.* **17**, 291–303. https://doi.org/10.1038/cdd.2009.124 (2010).
43. Stockwell, B. R. et al. Ferroptosis: A regulated cell death nexus linking metabolism, redox biology, and disease. *Cell* **171**, 273–285. https://doi.org/10.1016/j.cell.2017.09.021 (2017).
44. Shi, J. et al. Cleavage of GSDMD by inflammatory caspases determines pyroptotic cell death. *Nature* **526**, 660–665. https://doi.org/10.1038/nature15514 (2015).
45. Stephenson, K. et al. Updates on dietary models of nonalcoholic fatty liver disease: current studies and insights. *Gene Expr.* **18**, 5–17. https://doi.org/10.3727/105221617X15093707969658 (2018).
46. Yao, Z. M. & Vance, D. E. Reduction in VLDL, but not HDL, in plasma of rats deficient in choline. *Biochem. Cell. Biol.* **68**, 552–558. https://doi.org/10.1139/o90-079 (1990).
47. Mocciaro, G. et al. Non-alcoholic fatty liver disease is characterised by a reduced polyunsaturated fatty acid transport via free fatty acids and high-density lipoproteins (HDL). *Mol. Metab.* **73**, 101728. https://doi.org/10.1016/j.molmet.2023.101728 (2023).
48. Fisher, C. D. et al. Hepatic cytochrome P450 enzyme alterations in humans with progressive stages of nonalcoholic fatty liver disease. *Drug Metab. Dispos.* **37**, 2087–2094. https://doi.org/10.1124/dmd.109.027466 (2009).
49. Novaes, J. T. et al. Disposition, metabolism and histone deacetylase and acetyltransferase Inhibition activity of Tetrahydrocurcumin and other curcuminoids. *Pharmaceutics* **9** https://doi.org/10.3390/pharmaceutics9040045 (2017).
50. Ha, K. B. et al. EW-7197 attenuates the progression of diabetic nephropathy in db/db mice through suppression of fibrogenesis and inflammation. *Endocrinol. Metab. (Seoul).* **37**, 96–111. https://doi.org/10.3803/EnM.2021.1305 (2022).

Acknowledgements

The authors gratefully acknowledge the Government Pharmaceutical Organization (Bangkok, Thailand) for their generous contribution of Tetrahydocurcumin (THU).

Author contributions

K.B. conceptualization, methodology, data curation, formal analysis, writing – original draft, review, and editing the manuscript. E.S.L. methodology, formal analysis, writing – review and editing. S.H.J. methodology, writing – review and editing. N.W.P. methodology. S.B.L. methodology. C.H.C. conceptualization, funding acquisition,

supervision, writing – review and editing. All authors reviewed the manuscript.

Funding
This work was supported by the National Research Foundation of Korea (NRF) grant funded by the Korean Government (MSIT) (No. NRF- 2022R1I1A1A01068782) and the Ministry of Education (No. NRF-2021R1A2B5B01002354). This project was supported by the National Science Research and Innovation Fund (NSRF) under the Basic Research Fund of Khon Kaen University.

Declarations

Competing interests
The authors declare no competing interests.

Additional information
Supplementary Information The online version contains supplementary material available at https://doi.org/10.1038/s41598-025-23626-3.

Correspondence and requests for materials should be addressed to C.H.C.

Reprints and permissions information is available at www.nature.com/reprints.

Publisher's note Springer Nature remains neutral with regard to jurisdictional claims in published maps and institutional affiliations.